Hydrogen-assisted microcrack formation in bearing steels under rolling contact fatigue

X.Z. Liang[a], G.-H. Zhao[a], J. Owens[a], P. Gong[b], W.M. Rainforth[b], P.E.J. Rivera-Díaz-del-Castillo[a],[*]

[a] Department of Engineering, Lancaster University, Lancaster LA1 4YW, UK
[b] Department of Materials Science and Engineering, The University of Sheffield, Sheffield S1 3JD, UK

ARTICLE INFO

ABSTRACT

A ball-on-rod RCF tester was employed to investigate the failure mechanisms of hydrogen-rich rolling components. The formation of defects, voids and surface cracks is significantly facilitated in hydrogen-rich bearing steels. In samples with RCF cycles of 1.6×10^7, the void density in hydrogen-rich samples is about three times that of hydrogen-free samples, whilst their crack length density four times that of hydrogen-free samples. This is due to a higher stress intensity factor around inclusions which is altered by hydrogen. Further characterisation confirms that grain boundaries are preferential sites for void formation and crack propagation.

1. Introduction

Bearing steels are typically martensitic grades featuring high wear resistance and superior rolling contact fatigue endurance [1,2]. For example, high carbon 100Cr6 is a bearing grade which has been applied to wind turbines, automobiles and aerospace products. However, failure in bearing steels can be facilitated by increasing contact pressure, temperature and hydrogen ingress [3–5]. These factors are believed to accelerate microstructural decay and thus degrade mechanical properties.

Rolling contact fatigue (RCF) is a key factor to assess the service life of bearing parts subjected to a high contact pressure and rotational speed [2]. RCF failures can be induced either from the surface or the subsurface [2]. Surface-induced RCF failure appears at the very early stages of bearing life, and is greatly affected by conditions of surface roughness and oil film thickness. In practice, this type of failure can be eliminated by proper lubrication during service [2]. In contrast, subsurface induced RCF failure is not avoidable and limits the long-term service life. Subsurface induced RCF often involves microstructural alterations, for example, the formation of white etching areas, dark etching regions and white etching bands [1,6,7]. The presence of such alterations in bearings assists the formation and propagation of subsurface cracks.

It is well-known that mechanical properties can be significantly decreased by hydrogen [3,8–11]. In bearing parts, hydrogen can be introduced in several ways, such as lubricant decomposition, materials processing, general corrosion and internal decarburisation [3]. Such hydrogen ingress can result in a significant decrease of service life [3,4,10,11]. Szost et al. [4] reported that a hydrogen-rich 100Cr6 bearing sample failed after 2.03×10^7 RCF cycles whose failure is much faster than the hydrogen-free sample in which no failure appeared even after 1.6×10^8 RCF cycles. It was also reported that white etching areas are present in a failed hydrogen-rich 100Cr6 sample after only 2.03×10^7 RCF cycles, whereas they occur in hydrogen-free samples after 10^8 cycles [4]. The presence of white etching areas is thought to assist the development of subsurface cracks.

Several mechanisms have been established to rationalise hydrogen embrittlement. Hydrogen enhanced decohension (HEDE) was firstly proposed by Troiano et al. [12,13] in the 1950s and follow-up developments were progressed by Oriani and co-workers [14,15]. In this scenario, hydrogen was trapped and accumulated within the gaps of a lattice, with such accumulation leading to weakening of the lattice coherent bonding. Then the cracks are being initiatied and propagated. Hydrogen enhanced localised plasticity (HELP) is proposed based on the TEM observation that dislocations pile-up ahead of a crack tip in the presence of hydrogen [16,17]. This produces a high stress concentration ahead of the crack tip which then propagates. Although a combination of mechanisms could be considered to account for hydrogen emrbittlement in different materials, it is suggested that the HEDE is dominant in high strength materials whilst HELP is more common in low strength materials [18,19].

Bearings possess high yield strength and high hardness. For 100Cr6 bearings, Yamabe et al. [20] reported that secondary cracks can be greatly facilitated in the presence of hydrogen. The coalescence of

---

[*] Corresponding author.
E-mail address: p.rivera1@lancaster.ac.uk (P.E.J. Rivera-Díaz-del-Castillo).

Table 1
Chemical composition of the investigated steels.

Element	C (wt.%)	Cr (wt.%)	Ni (wt.%)	Mn (wt.%)	Si (wt.%)	Mo (wt.%)	Cu (wt.%)	P (ppm)	S (ppm)
	0.95	1.50	0.02	0.01	0.27	0.01	0.02	130	20
Al (ppm)	Ti (ppm)	Ca (ppm)	Pb (ppm)	Sn (ppm)	As (ppm)	Sb (ppm)	Bi (ppm)	N (ppm)	O (ppm)
247	6	2	16	10	20	10	30	20.3	6.1
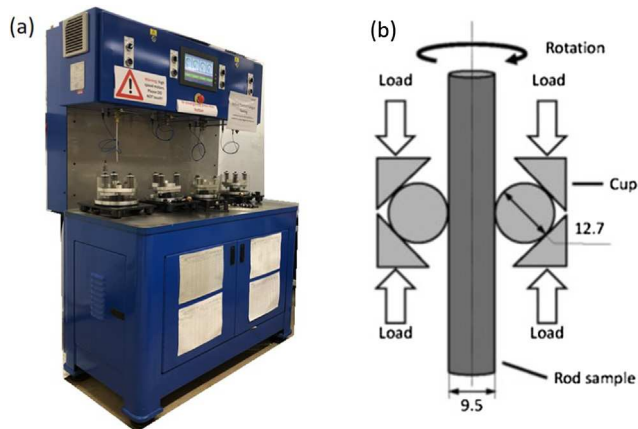
Fig. 1. (a) Three ball-on-rod rolling contact fatigue tester; (b) Principle of ball-on-rod rolling contact fatigue tests.

secondary cracks, which formed ahead of primary cracks, can dramatically facilitate the propagation of the primary crack; such coalescence forms a long crack which could lead to hydrogen-assisted fatigue premature failure. Therefore, such phenomenon implies that HEDE rules the hydrogen-assisted fatigue failure in bearings. In this study, systematic RCF tests were performed on bearings in the presence of hydrogen with the aim to investigate the mechanism of hydrogen-assisted RCF failure in bearings.

2. Experiment methods

2.1. Materials

Bearing grade 100Cr6 (SAE 52100) was investigated in this study. Table 1 lists its chemical composition as measured by optical emission spectroscopy. The specimens were first quenched from an austenitisation temperature of 840 °C to room temperature and tempered at 160 °C for 90 min. Rod samples with 9.53 mm diameter were prepared for rolling contact fatigue tests. Surface roughness of 0.12 μm was measured for tested rod specimens.

2.2. Hydrogen charging

Hydrogen charging was electrochemically performed in a 3.5 wt% NaCl solution at 80 °C heating. Hydrogen charging duration was 5 days at a current density of 10 mA/cm². The choice for 10 mA/cm² demonstrated negligible surface corrosion so that surface-initiated fatigue was avoided. Szost et al. [4] have shown that the 100Cr6 rod samples can reach hydrogen saturation of 5 ppm after 24 h hydrogen charging. In this study, thermal desorption analysis measurements were conducted after 3, 5 and 7 days indicating hydrogen saturation of 5 ppm by 5 days charging. Therefore, the 5 days charging can introduce sufficient hydrogen to reach saturation status (≥ 5 ppm). In addition, it has been shown that the hydrogen charging has a minor effect on surface roughness which plays insignificant role in rolling contact fatigue

failure [21]. In this study, the paint (Lacomit varnish) was used to cover the remaining part of sample to reduce corrosion. When hydrogen charging finished, ethanol was used to clean the sample immediately, and Lacomit remover was used to remove the paint. The RCF rig was calibrated and prepared for fixing the sample before the finish of hydrogen charging. A total time of about 30 min is adopted before the RCF test. De-trapping of diffusible hydrogen in the first few hours after stopping charging is significant, so it is expected to lose a part of the total charged hydrogen between taking samples out of the charging cell and starting the RCF test. However, the hydrogen in the sample centre will slowly diffuse to the sample surface sustaining a moderate hydrogen level towards the sample surface. It can be found in Ref. [21] that a small amount of diffusible hydrogen content can still be measured throughout testing: 1.37–1.54 ppm at 0 h effusion time and 0.26–0.40 ppm after 208 h test. Therefore, for the tests in this study, part of hydrogen will stay in the sample after setup and test.

2.3. Rolling contact fatigue test

Rolling contact fatigue testing was performed on a three ball-on-rod fatigue tester. Fig. 1(a) shows the three-ball-on-rod RCF tester and Fig. 1(b) shows the principle of ball-on-rod test. RCF is introduced by the contact of three balls, and is controlled by the load applied on the ball cup during the rotation of the rod sample. The material of the balls is the same as that of rod samples. The test is performed at room temperature whilst the temperature of the sample during testing ranges between 35 and 40 °C. Turbo oil (BP Turbo Oil 2380) is used for lubrication at a feeding rate of 10 drops per minute. In this study, a maximum contact pressure of 3.2 GPa was applied at a rotational speed of 3600 rpm, which corresponds to a stress cycle frequency of 9000 cpm. RCF cycles up to 7.3×10^5 and 1.6×10^7 were applied on samples to show the evolution of hydrogen-assisted crack development. A total number of six samples were prepared as listed in Table 2.

2.4. Hardness

Hardness tests were performed on circumferential sections of samples from surface towards the centre with a contact force of 1 kgf. An indentation map of 5×4 was performed on samples to obtain a hardness profile from sample surface to a depth of about 600 μm. A discussion of hardness variation is presented in Section 3.2.

2.5. Microstructural characterisation

Time-of-flight neutron diffraction technique is a fast and accurate

Table 2
RCF samples tested in this study.

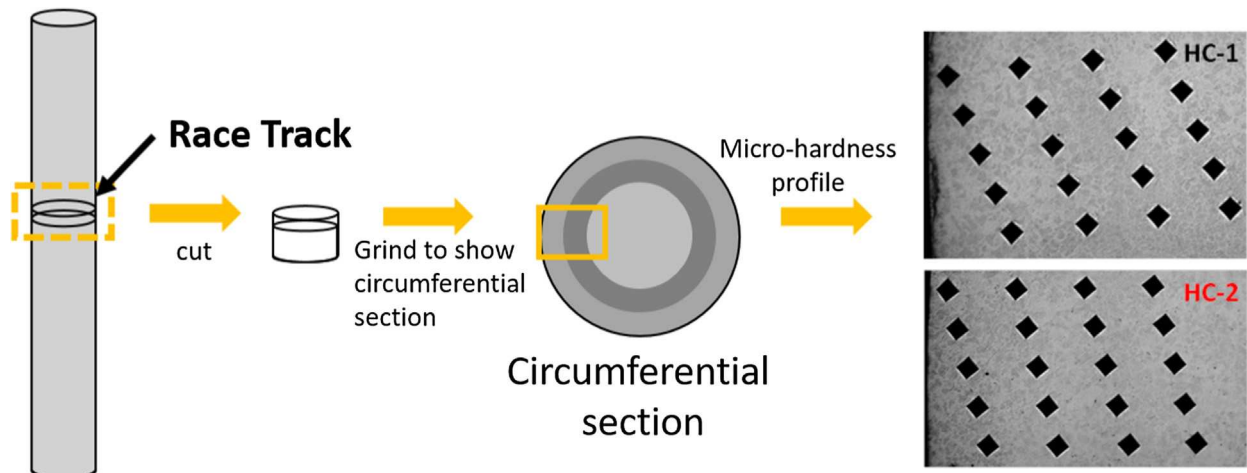| Hydrogen condition	RCF revolution		
	0	7.3×10^5	1.6×10^7
Hydrogen free	HF-0	HF-1	HF-2
Hydrogen charged	HC-0	HC-1	HC-2

Fig. 2. Schematic diagram of sample preparation and hardness indents performed on RCF samples.

diffractometry technique to probe the microstructure information from the bulk [9,22,23]. In this study, Time-of-flight neutron diffraction experiments were performed on the ENGIN-X neutron diffractometer, ISIS, UK, to identify the phases. A gauge volume of $4 \times 4 \times 4\,mm^3$ was set for the neutron diffraction.

After the hydrogen charging and RCF tests, the samples were machined along the circumferential section of the RCF track to examine the cracks, as shown in Fig. 2. To prepare the samples for optical microscope characterisation, sample surfaces were ground and polished down to 1 μm following 2% nital etching to reveal the microstructure.

To prepare the sample for EBSD, a further ion milling was performed using GATAN PECS II to clean the surface. EBSD was performed on a FEI NOVA NANOSEM 450 at 20 keV acceleration voltage with an Oxford EBSD detector. A scanning step size of 100 nm was applied. Screen binning of 4 by 4 was applied to optimise the EBSD scanning time.

3. Results and discussion

3.1. Microstructure

100Cr6 bearings typically consist of a martensite matrix, with retained austenite and carbides as precipitates. Fig. 3 shows a neutron diffraction pattern obtained from the hydrogen-free sample, together with an optical image to show the microstructure. The results show both martensite (α') and retained austenite (γ) phases are clearly identified and a small peak was identified from the contribution of Fe_3C. The morphology of Fe_3C is revealed as small particles embedded in the matrix.

3.2. Stress distribution and micro-hardness profile

It has been reported that a micro-hardness variation is associated with the applied cyclic stresses under rolling contact fatigue [24]. The applied stress introduces a plastic strain and induces microstructural alterations under RCF. The accumulation of plastic strain results in hardening due to the multiplication of dislocations. Microstructural alterations may have different effects on hardness. The formation of white etching areas is reported to increase the local hardness due to the formation of dislocation cell walls, whilst the presence of dark etching regions reduced the hardness [6,7,25]. Such microstructural alterations will result in a change of the hardness profile. Fig. 4(a) shows the micro-hardness profiles in samples HC-1 and HC-2. An increase in hardness is obtained at depth ranged from 100 to 200 μm in both samples. As a greater number of RCF cycles is achieved in HC-2 sample, the difference of ΔH_V is greater in HC-2 sample. In this study, no
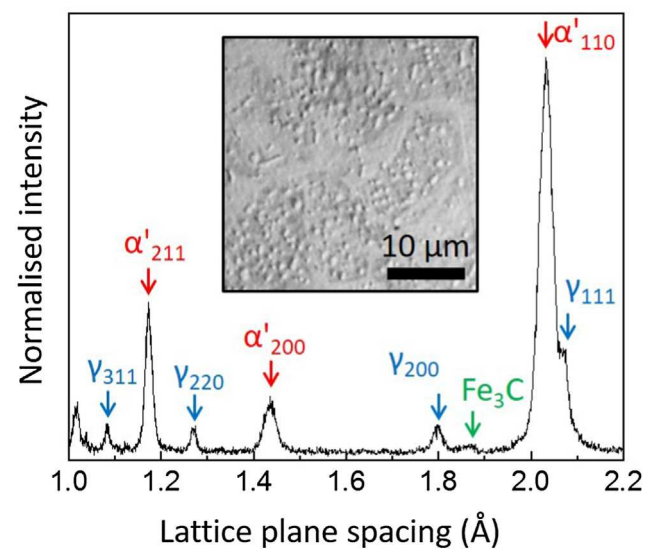

Fig. 3. Neutron diffraction spectrum pattern of 100Cr6 rod sample; diffraction peaks of martensite (α'), retained austenite (γ) and Fe_3C are observed; the optical image shows that Fe_3C particles embedded in the martensite matrix.

obvious microstructural alterations have been observed. The increase in micro-hardness is mainly due to strain accumulation under rolling contact fatigue. Fig. 4(b) shows the shear stress distribution beneath the surface. The calculation procedure is shown in Appendix A. It should be noted that the sliding effect was not considered here, as sliding has minor effects to correlate the shear stress with the hardness variation in this study. It can be seen that the applied peak shear stress is estimated to be at around 200 μm. The reduction of the shear stress is realised at deeper regions and the stress-affected region reaches about 500 μm in depth. The variation of hardness profiles and stress distribution is in agreement.

3.3. H-assisted crack formation under RCF

3.3.1. H-assisted crack propagation

In 100Cr6 bearing steel, several types of inclusions are present such as MnS, Al_2O_3, SiO_2 and TiN [26]. Their size ranges from 2 to ~10 μm [27]. As inclusions typically have weak bonding with the matrix, they frequently serve as initiation sites for both microstrucutral alterations and crack development [26,27]. In this study, optical microscopy was used to measure the crack length and depth; some of the corresponding
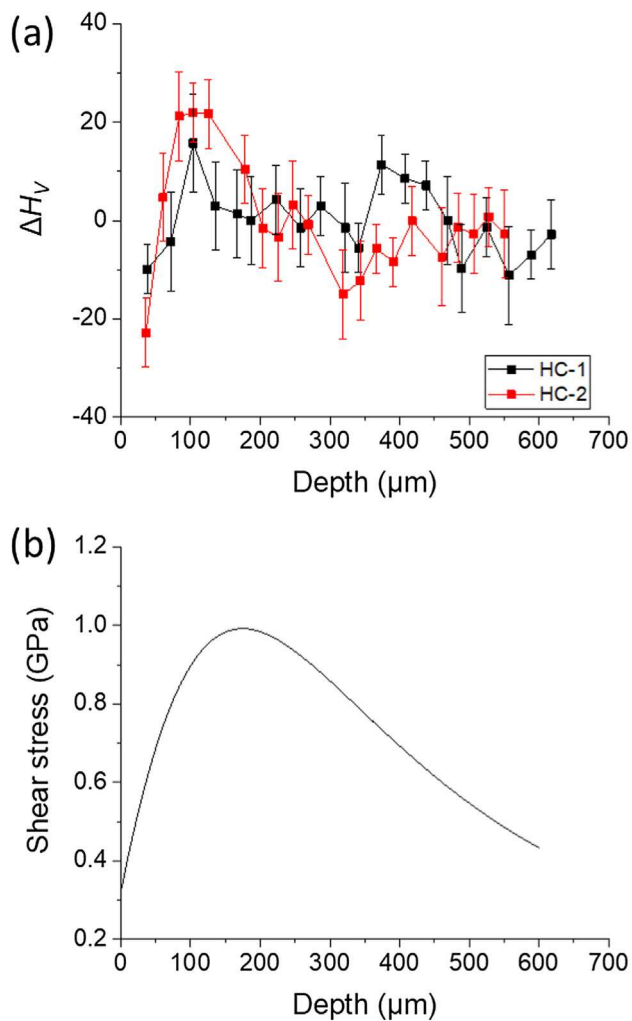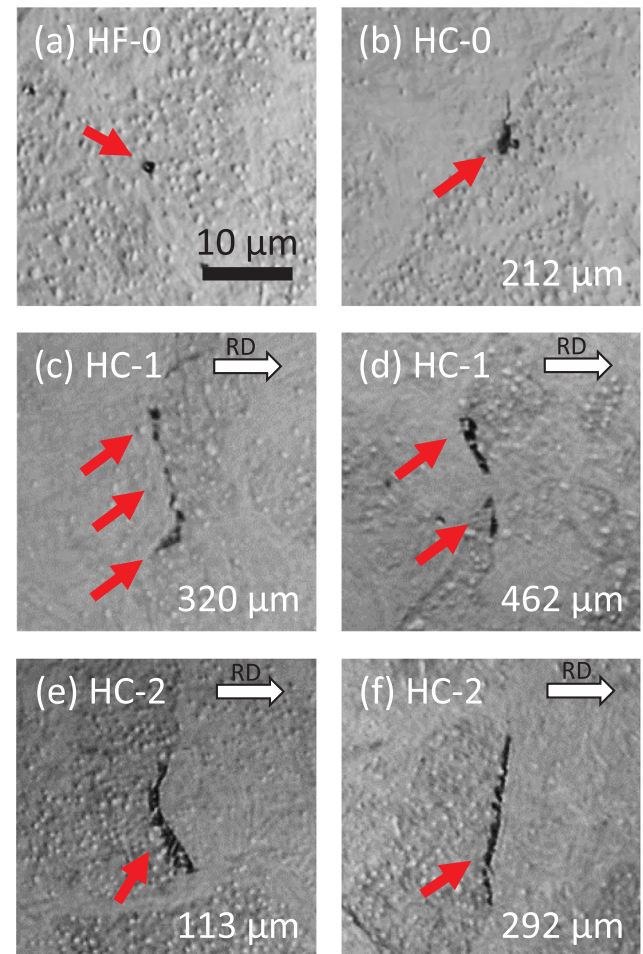
Fig. 4. Relation between hardness and subsurface stress distribution. (a) hardness profiles of samples HC-1 and HC-2 from the sample surface towards the centre; error estimation of hardness is achieved by multiple reading; (b) calculated shear stress distribution along the depth.

Fig. 5. Optical images showing the development of hydrogen-assisted grain boundary crack (a) typical inclusion in hydrogen-free sample; (b) small crack developed from a inclusion in hydrogen charged sample; (c) and (d) are hydrogen-assisted grain boundary cracks developed in hydrogen-rich sample with 7.3×10^5 RCF cycles; (e) and (f) are well-developed hydrogen-assisted grain boundary cracks in hydrogen-rich sample with 1.6×10^7 RCF cycles; the number displayed on the right bottom corner indicates the depth of the crack present beneath the surface. RD means rolling direction.

images are showed with the associated inclusions and their surrounding cracks. In hydrogen-free samples, inclusions are homogeneously distributed and crack development can rarely be observed, which has been studied in reference [26]. Fig. 5(a) shows a typical inclusion in the hydrogen-free condition. Fig. 5(b) shows a typical H-assisted crack development from an inclusion by hydrogen charging. This is due to residual stresses present around the inclusion. By applying RCF cycles on hydrogen-rich samples, cracks are initiated and further developed. Fig. 5(c) and (d) shows some developed cracks within HC-1 sample. Besides, the result implies that the crack development has a preferential direction that propagates along grain boundaries. This preferential crack development may be due to a high hydrogen concentration at grain boundaries. Further EBSD experiments have been performed and the results are in the following section. By applying higher RCF cycles, as 1.6×10^7 in HC-2 sample, more developed cracks can be observed and some of them are fully developed along grain boundaries, as shown in Fig. 5(e) and (f). Such developed cracks in hydrogen-rich samples rarely appear in hydrogen-free samples.

3.3.2. EBSD characterisation of cracks along grain boundaries

Fig. 6 shows a small void in HC-2 sample. It can be seen that the void is located at a grain boundary, as shown in Fig. 6(c). Fig. 7 shows a typical EBSD result obtained from HC-2 sample. Fig. 7(a) shows the morphology of a crack located in the middle of the scan region.

Fig. 7(b) shows the band contrast map. There is no obvious band contrast variation in vicinity of the crack, which suggests this crack is a brittle-type opening. It should be noted here that both the depth and width of material which contributed to EBSD diffraction signal is about tens of nanometre [28]. However, the depth and the width of these microcracks are shallow and narrow, and they are of the same order of magnitude than the EBSD pixel size. Hence, when the EBSD pixel is located on the microcrack, the adjacent material will contribute to the diffraction signal. Therefore, it is not possible to use such EBSD pixels to characterise the crack orientation in the corresponding EBSD map. Fig. 7(c) shows the inverse pole figure map. On the two sides of the crack, a distinct grain orientation is measured which suggests that this crack propagates along a grain boundary. In addition, as there is no obvious band contrast variation in vicinity of the crack, the result implies that HEDE may contribute to the development of subsurface cracks in bearings.

To have a better understanding of where the microcracks formed, a larger EBSD map was obtained, as shown in Fig. 8. As the sample surface was cleaned by ion milling, the edges of microcracks were affected which appears not as sharp, as they were imaged by nital etching. Here, three microcracks were identified. It can be seen that the crack development is mostly along boundaries. Kurten et al. [29] investigated
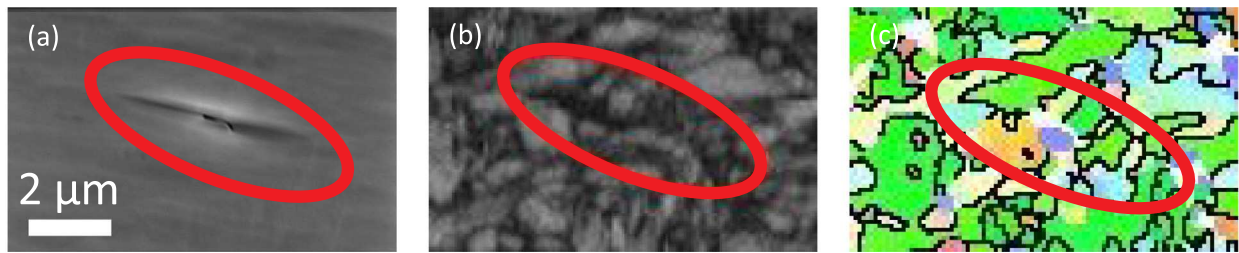
Fig. 6. An EBSD map shows a small void in HC-2 sample: (a) Secondary electron image showing the morphology of the void; (b) Band contrast map; (c) IPF colour map.
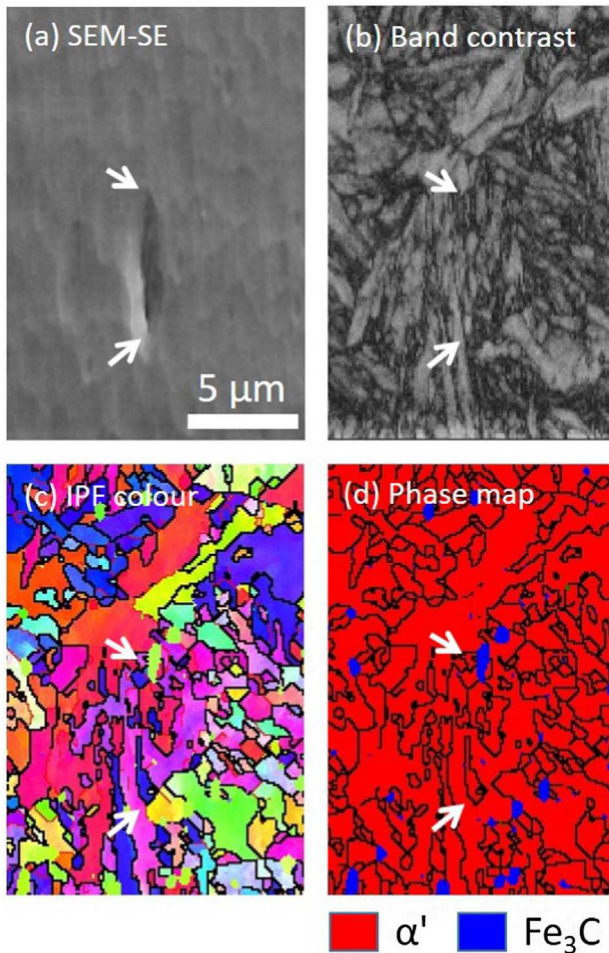

Fig. 7. EBSD result of a hydrogen-assisted crack in hydrogen-rich sample with 1.6×10^7 RCF cycles: (a) Secondary electron image showing the morphology of crack; (b) Band contrast map; (c) IPF colour map and (d) Phase map showing the distribution of martensite (α') and Fe_3 C; arrows point the ends of the crack.

hydrogen-assisted rolling contact fatigue. Main cracks appeared close to the surface and transgranular cracks appeared to be dominant. While in deeper regions, some of the intergranular cracks appeared especially at crack tips. Such results match the observation in this study that intergranular microcracks can be facilitated by hydrogen.

3.4. Void formation and crack propagation in hydrogen-rich RCF samples

To have statistics of the developed cracks in these samples, the densities of voids and crack length were measured within the subsurface region. A criterion is defined here: voids are the size of defects lower than 2 μm whilst the cracks represent the length of defects that are longer than 2 μm. A void density is obtained by the counts of defects over measurement region whilst a crack length density is calculated by total crack length divide measurement region.

3.4.1. H-assisted void formation

Fig. 9(a) shows the measurement of void density in these samples. The hydrogen pre-charge induces a small amount of increase in void density in 100Cr6 bearings steel. Such increase kept same trend in HC-1 sample. However, with 1.6×10^7 RCF cycles in HC-2 sample, the void density increases dramatically to 833 count/mm^2 which is about 3 times that of HF-2 sample.

3.4.2. H-assisted crack propagation

Fig. 9(b) shows the measurement of crack length density in the samples. In hydrogen-free samples, it is believed that fatigue cracks shall not be facilitated within the early RCF cycles ($< 10^8$ RCF cycles) in these samples. Therefore, the hydrogen-free samples have a low crack length density lower than 300 μm/mm^2. It is worth noting that a crack length density of 300 μm/mm^2 may represent the ground density of pre-existing large defects in the material. By comparing the hydrogen-free and hydrogen-rich samples, an increase of crack length density was observed. In this study, a four-fold crack length density was measured in HC-2 sample compared with HF-2 sample. Vegter et al. [30] reported that small cracks were present in hydrogen charged bearings after 2.6×10^5 revolutions. They described that these cracks are too small to be properly documented. However, in this study, it is found that these cracks can be revealed by a proper etching (slightly under-etching) which can clearly reveal the outline of these cracks under optical microscope.

3.5. Effect of hydrogen on the stress intensity factor

In the hydrogen-free case, the equivalent stress intensity factor (SIF) for cracks on ball-on-rod bearing is [31]

$$K_{eq}^{HF} = f(p_0, X_D, \phi, a), \tag{1}$$

where p_0 is the applied contact pressure, X_D is the normalized lateral position between the centre of contact patch and the centre of crack, ϕ is the angle between the perpendicular line to contact path and the orientation of crack, a is the initial crack size. Hydrogen introduction will not alter these values. In the hydrogen charged scenario, the effective SIF is altered and can be estimated by introducing a hydrogen-induced influence factor λ [32]

$$K_{eq}^{HC} = \lambda K_{eq}^{HF}. \tag{2}$$

In the scenario of rotating bending fatigue test, the factor λ can be determined by the following empirical expression [32]

$$\lambda = 1 + 0.09 \times C_H^2, \tag{3}$$

where C_H is hydrogen concentration in wppm. It has been reported the saturation of hydrogen is about 5 ppm in 100Cr6 [4]. Therefore, if we assume that this calculation of λ is valid in the rolling contact fatigue scenario, the hydrogen-affected stress intensity factor $\lambda = 1 + 0.09 \times C_H^2 = 3.25$ can be applied. According to the crack growth
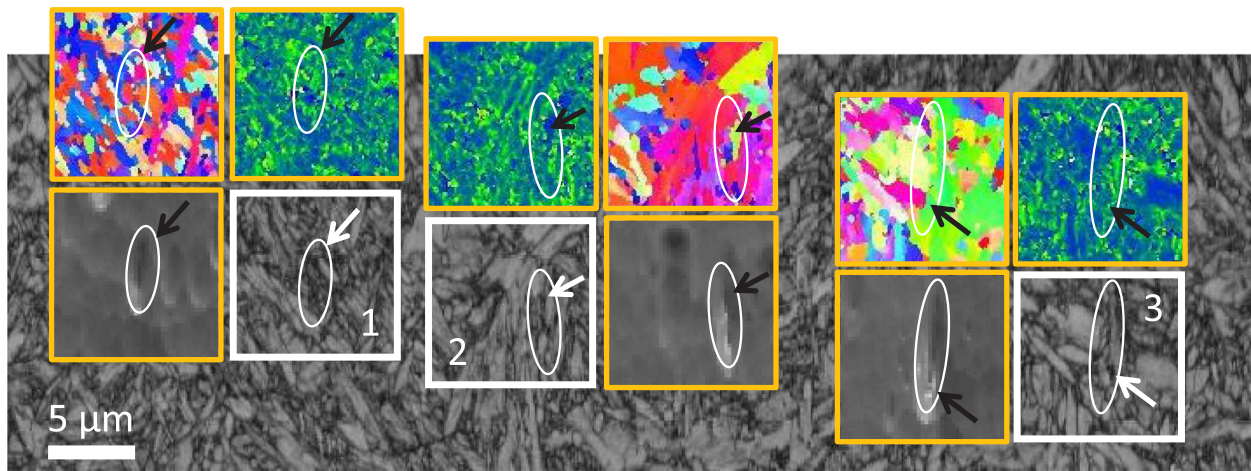
Fig. 8. EBSD map showing hydrogen-assisted microcracks in hydrogen-rich sample with 1.6×10^7 RCF cycles; for each microcrack, the corresponding IPF color map, misorientation map (range 0–2) and SEM image are displayed.
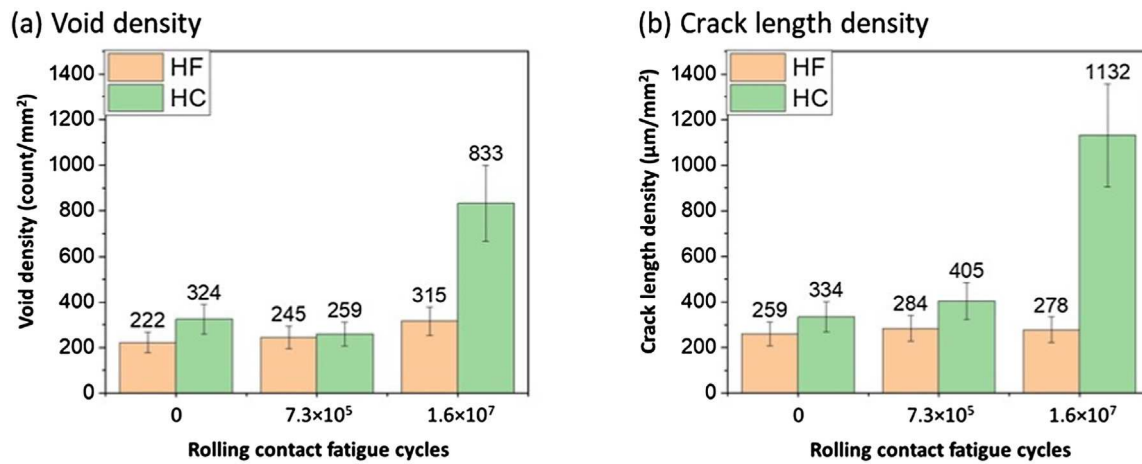

Fig. 9. Measurement result of crack length density in these samples; voids are considered to be lower than 2μ m whilst the cracks represent the length of defects longer than 2μ m. Void density is measured according to the total number of voids divided by unit area; crack length density is measured according to the total length of cracks divided by unit area.

criterion $K_{eq} > K_{th}$, the crack propagation has much higher chance to be facilitated with hydrogen being present.

3.6. Mechanism of H-assisted premature failure in RCF

The results suggest that both voids and cracks are greatly facilitated under RCF by hydrogen. The diffusion mechanism for hydrogen is a random walk across interstitials and vacancies, with the hydrogen-vacancy being significant to hydrogen embrittlement. It has been reported that the density of vacancy can be facilitated by hydrogen [33,34]. Using first-principle simulations, Momida et al. [34] reported that hydrogen and vacancies prefer to accumulate as VaH complexes adjacent to grain boundaries in iron, and the accumulation of vacancy-hydrogen (VaH) complexes can effectively reduce the strength of grain boundaries. Xie et al. [35] reported that the presence of VaH complexes can inhibit dislocation mobility at the low stress state, however, the VaH complexes may encounter a shakedown when dislocations glide through under a highly stressed state. Such shakedown of VaH complexes could result in material damage which results in micro-voids formation and coalescence. In martensitic steels, a high concentration of hydrogen and localised stress can be present at grain boundaries. Such accumulation can result in an increase in void formation under rolling contact fatigue. Thereafter the coalescence of voids can be realised with the evolution of RCF, and thus hydrogen-assisted subsurface cracks are facilitated in bearings. These cracks can lead to premature fatigue failure under rolling contact fatigue.

Based upon the above discussion, a mechanism of H-assisted grain boundary crack can be proposed for the steels under rolling contact fatigue in this study. A schematic illustration is shown in Fig. 10. The evolution of hydrogen induces void formation in the hydrogen-rich sample together with precipitates and voids originally present in the material, can act as initiation sites for cracks. As grain boundaries have a higher hydrogen concentration and localised stress, they are prone to facilitate crack propagation. With the evolution of rolling contact fatigue cycles, coalescence of voids evolves into grain boundary cracks. As a result, the increased amount of grain boundary cracks formed under rolling contact fatigue leads to premature failure in hydrogen-rich martensitic bearing steels.

4. Conclusion

In this study, hydrogen-assisted cracking is studied in bearing steels under rolling contact fatigue. The key findings are as follows:

- Rolling contact fatigue tests were performed on hydrogen-free and hydrogen-rich samples, and subjected to different level of rolling contact fatigue cycles. By quantifying the densities of void and crack length in these samples, it is found that hydrogen can dramatically
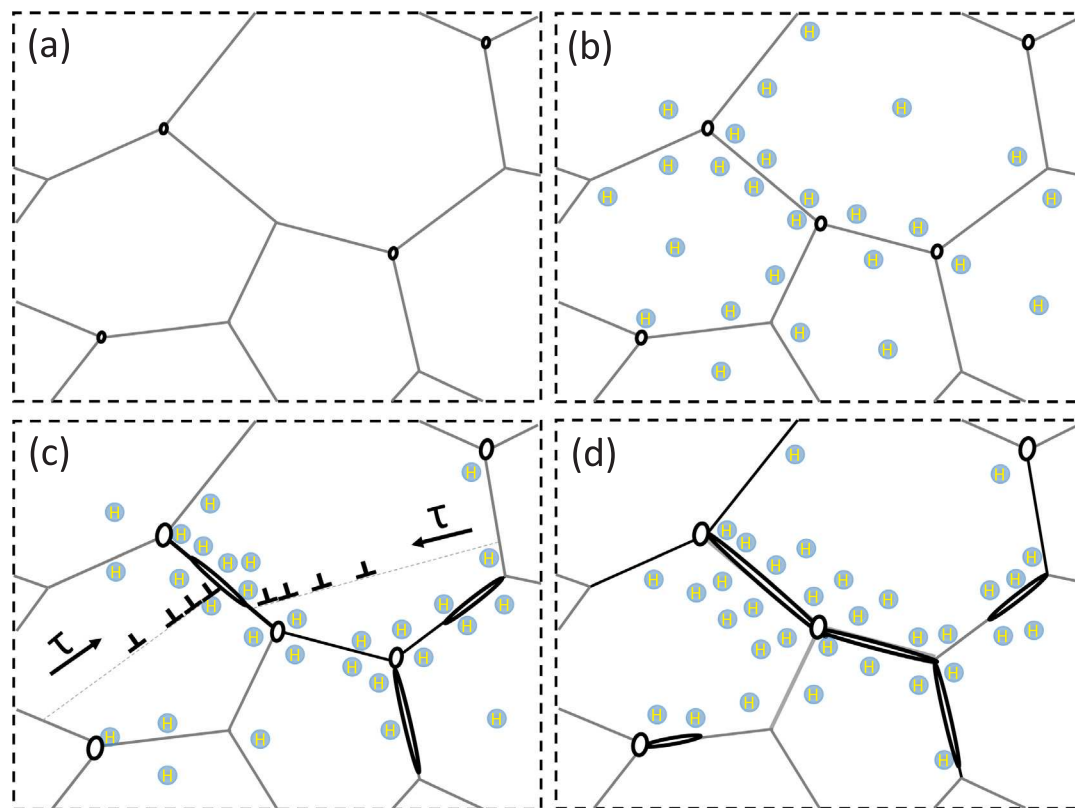
Fig. 10. Schematic diagram of void formation and crack propagation with hydrogen under rolling contact fatigue: (a) a few small defects exist in original materials before hydrogen ingress; (b) hydrogen ingress induces an increase of small defects; (c) a few defects developed as micro-cracks in early stage RCF; (d) formation of intergranular cracks with further RCF revolution.

facilitate the formation of such defects: in hydrogen-rich sample with rolling contact fatigue cycles of 1.6×10^7, the void density in hydrogen-rich samples is about three times that of hydrogen-free samples, whilst the crack length density in hydrogen-rich sample is four times that of hydrogen-free samples. The development of such cracks has not been observed in the hydrogen free sample by applying same levels of rolling contact fatigue cycles.

- Typical hydrogen-assisted cracks were characterised in hydrogen-rich samples. It is found that a group of voids can be formed in the early stage of rolling contact fatigue. With the evolution of rolling contact fatigue, the coalescence of voids can be realised, thus hydrogen-assisted subsurface cracks can be formed in bearings. These cracks could lead to premature fatigue failure, which is critical to rolling contact fatigue. In addition, both optical microscope images and EBSD results show that grain boundaries are the preferential sites for the formation of such defects which may due to the higher hydrogen concentration and localised stress at grain boundaries.
- A qualitative analysis of hydrogen influence on stress intensity

factor is applied to interpret the hydrogen-assisted cracking in bearings. The stress intensity factor could be three times with hydrogen, which can provide a higher probability for crack propagation. A detailed quantitative analysis is needed in the future.

Declaration of Competing Interest

The authors declare that they have no known competing financial interests or personal relationships that could have appeared to influence the work reported in this paper.

Appendix A. Subsurface stress calculation

In this study, three-ball-on-rod RCF tests were performed. An elliptical contact patch occurs between the rod and balls. The theoretical calculation can be found in Ref. [36]. The tester and the schematic setup is shown in Fig. 1. Fig. A11 shows the schematic diagram of the contact between ball and rod. An ellipticity parameter can be calculated by
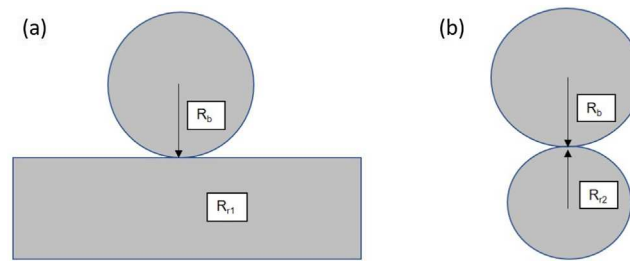
$$k = a/b = (R_A/R_B)^{2/3} \tag{A.1}$$

where $R_A = 0.25 \times \left(\frac{2}{R_b} + \frac{1}{R_{r1}} + \frac{1}{R_{r2}} \right) - 0.25 \times$ and $R_B = \left(\frac{2}{R_b} + \frac{1}{R_{r1}} + \frac{1}{R_{r2}} \right)$. For the RCF setup in this study, the following values are used: $R_b = 6.35$ mm, $R_{r1} = 4.77$ mm and $R_{r2} = 10$ m. A contact factor can be calculated by

$$c = (ab)^{1/2} = \left(\frac{3FR_e}{4E^*} \right)^{1/3} F_1(R_A/R_B) \tag{A.2}$$

where F is the applied force between ball and rod. Here, a force of 205 N is applied to obtained the maximum contact pressure 3.2 GPa. The relative

Fig. A11. Schematic of the contact between ball and rod: (a) side view and (b) front view. R_b denotes the radius of the ball, R_{r1} and R_{r2} represent the radius of rod on two directions.

curvature is calculated by $R_e = (R_A R_B)^{1/2}$. F_1 is the geometry factor and equals to 0.989 for the setup in this study. The reduced modulus E^* can be expressed by

$$\frac{1}{E^*} = \frac{1 - v_b^2}{E_b} + \frac{1 - v_r^2}{E_r}.$$

(A.3)

Elastic modulus $E_b = E_r = 210$ GPa and Poisson's ratio $v_b = v_r = 0.3$ was applied for both balls and rods. The length of the principal elliptical contact patch semi-axis can be calculated by $a = c \times \sqrt{k}$ and $b = c/\sqrt{k}$. For the maximum contact pressure $P_0 = 3.2$ GPa, it can be calculated that $a = 232\,\mu m$ and $b = 132\,\mu m$. Using the size of the contact patch, a shear stress distribution model could be produced. The equations that were used for the distribution are

$$\sigma_z = -\left(1 + \frac{z^2}{a^2}\right)^{-1} \times P_0$$

(A.4)

$$\sigma_\theta = \left(-(1 + v) \times \left(1 - \left(\frac{z}{a}\right) \times \tan^{-1}\left(\frac{a}{z}\right)\right) + 0.5 \times \left(1 + \frac{z^2}{a^2}\right)^{-1}\right) \times P_0$$

(A.5)

$$\tau = 0.5 \times |\sigma_z - \sigma_\theta|$$

(A.6)

where σ_z and σ_θ are the principle stresses in the subsurface. z is the depth below the surface and τ is the shear stress.

References

[1] Fu H, Galindo-Nava EI, Rivera-Díaz-del-Castillo PEJ. Modelling and characterisation of stress-induced carbide precipitation in bearing steels under rolling contact fatigue. Acta Mater 2017;128:176–87.

[2] Bhadeshia HKDH. Steels for bearings. Prog Mater Sci 2012;57(2):268–435.

[3] Stopher MA, Rivera-Díaz-del-Castillo PEJ. Hydrogen embrittlement in bearing steels. Mater Sci Technol 2016;32(11):1184–93.

[4] Szost BA, Rivera-Díaz-del-Castillo PEJ. Unveiling the nature of hydrogen embrittlement in bearing steels employing a new technique. Scr Mater 2013;68(7):467–70.

[5] Jelita Rydel J, Toda-Caraballo I, Guetard G, Rivera-Díaz-del-Castillo PEJ. Understanding the factors controlling rolling contact fatigue damage in VIM-VAR M50 steel. Int J Fatigue 2018;108:68–78.

[6] Fu H, Song W, Galindo-Nava EI, Rivera-Díaz-del-Castillo PEJ. Strain-induced martensite decay in bearing steels under rolling contact fatigue: modelling and atomic-scale characterisation. Acta Mater 2017;139:163–73.

[7] Fu H, Rivera-Díaz-del-Castillo PEJ. A unified theory for microstructural alterations in bearing steels under rolling contact fatigue. Acta Mater 2018;155:43–55.

[8] Bhadeshia HKDH. Prevention of hydrogen embrittlement in steels. ISIJ Int 2016;56(1):24–36.

[9] Liang XZ, Dodge MF, Kabra S, Kelleher JF, Lee TL, Dong HB. Effect of hydrogen charging on dislocation multiplication in pre-strained super duplex stainless steel. Scr Mater 2018;143:20–4.

[10] Uyama H, Yamada H, Hidaka H, Mitamura N. The effects of hydrogen on microstructural change and surface originated flaking in rolling contact fatigue. Tribology Online 2011;6(2):123–32.

[11] Kino N, Otani K. The influence of hydrogen on rolling contact fatigue life and its improvement. JSAE Rev 2003;24(3):289–94.

[12] Morlet JG, Johnson HH, Troiano AR. A new concept of hydrogen embrittlement in steel. Wright Air Development Center, Air Research and Development Command, United States Air Force; 1957.

[13] Troiano AR. The role of hydrogen and other interstitials in the mechanical behavior of metals. Trans ASM 1960;52(1):54–80.

[14] Oriani RA. The diffusion and trapping of hydrogen in steel. Acta Metall 1970;18(1):147–57.

[15] Oriani RA. A mechanistic theory of hydrogen embrittlement of steels, Berichte der Bunsengesellschaft für physikalische. Chemie 1972;76(8):848–57.

[16] Ferreira PJ, Robertson IM, Birnbaum HK. Hydrogen effects on the interaction between dislocations. Acta Mater 1998;46(5):1749–57.

[17] Robertson IM, Sofronis P, Nagao A, Martin ML, Wang S, Gross DW, et al. Hydrogen embrittlement understood. Metall Mater Trans A 2015;46(6):2323–41.

[18] Yousefi A, Itoh G. Tensile properties of an electrolytically hydrogen charged duplex stainless steel affected by strain rate. ISIJ Int 2018;58(3):561–5.

[19] Olden V, Thaulow C, Johnsen R. Modelling of hydrogen diffusion and hydrogen induced cracking in supermartensitic and duplex stainless steels. Mater Des 2008;29(10):1934–48.

[20] Yamabe J, Matsumoto T, Matsuoka S, Murakami Y. A new mechanism in hydrogen-enhanced fatigue crack growth behavior of a 1900-MPa-class high-strength steel. Int J Fract 2012;177(2):141–62.

[21] Evans MH, Richardson AD, Wang L, Wood RJK. Effect of hydrogen on butterfly and white etching crack (wec) formation under rolling contact fatigue (rcf). Wear 2013;306(1):226–41.

[22] Liang XZ, Zhao GH, Dodge MF, Lee TL, Dong HB, Rivera-Díaz-del-Castillo PEJ. Hydrogen embrittlement in super duplex stainless steels. Materialia 2020.

[23] Zhang RY, Qin HL, Bi ZN, Li J, Paul S, Lee TL. Using variant selection to facilitate accurate fitting of γ″ peaks in neutron diffraction. Metall Mater Trans A 2019;50(11):5421–32.

[24] Bhattacharyya A, Subhash G, Arakere N. Evolution of subsurface plastic zone due to rolling contact fatigue of M-50 NiL case hardened bearing steel. Int J Fatigue 2014;59:102–13.

[25] Su Y-S, Li S-X, Lu S-Y, Shu X-D. Deformation-induced amorphization and austenitization in white etching area of a martensite bearing steel under rolling contact fatigue. Int J Fatigue 2017;105:160–8.

[26] Fu H, Rydel JJ, Gola AM, Yu F, Geng K, Lau C, et al. The relationship between 100Cr6 steelmaking, inclusion microstructure and rolling contact fatigue performance. Int J Fatigue 2018.

[27] Hashimoto K, Fujimatsu T, Tsunekage N, Hiraoka K, Kida K, Santos EC. Effect of inclusion/matrix interface cavities on internal-fracture-type rolling contact fatigue life. Mater Des 2011;32(10):4980–5.

[28] Liang XZ, Dodge MF, Jiang J, Dong HB. Using transmission kikuchi diffraction in a scanning electron microscope to quantify geometrically necessary dislocation density at the nanoscale. Ultramicroscopy 2019;197:39–45.

[29] Kürten D, Khader I, Raga R, Casajús P, Winzer N, Kailer A, et al. Hydrogen assisted rolling contact fatigue due to lubricant degradation and formation of white etching areas. Eng Fail Anal 2019;99:330–42.

[30] Vegter RH, Slycke JT. The role of hydrogen on rolling contact fatigue response of rolling element bearings. J ASTM Int 2009;7(2):1–12.

[31] Pattabhiraman S, Levesque G, Kim NH, Arakere NK. Uncertainty analysis for rolling contact fatigue failure probability of silicon nitride ball bearings. Int J Solids Struct 2010;47(18):2543–53.

[32] Yang ZG, Li SX, Li YD, Liu YB, Hui WJ, Weng YQ. Relationship among fatigue life, inclusion size and hydrogen concentration for high-strength steel in the vhcf regime. Mater Sci Eng A 2010;527(3):559–64.

[33] Sugimoto H, Fukai Y. Hydrogen-induced superabundant vacancy formation by electrochemical methods in bcc Fe: Monte carlo simulation. Scr Mater 2017;134:20–3.

[34] Momida H, Asari Y, Nakamura Y, Tateyama Y, Ohno T. Hydrogen-enhanced vacancy embrittlement of grain boundaries in iron. Phys Rev B 2013;88(14):144107.

[35] Xie D, Li S, Li M, Wang Z, Gumbsch P, Sun J, et al. Hydrogenated vacancies lock dislocations in aluminium. Nat Commun 2016;7:13341.

[36] Johnson KL, Johnson KL. Contact mechanics. Cambridge University Press; 1987.